ACS APPLIED MATERIALS & INTERFACES

www.acsami.org

Research Article

Electrochemical Performance of Polymer-Derived Silicon-Oxycarbide/Graphene Nanoplatelet Composites for High-Performance Li-Ion Batteries

Gangadhar Jella,[⊥] Dillip K. Panda,[⊥] Nawraj Sapkota, Michelle Greenough, Santanu P. Datta, Apparao M. Rao, Ravindran Sujith, and Rajendra K. Bordia*

Cite This: *ACS Appl. Mater. Interfaces* 2023, 15, 30039−30051

Read Online

ACCESS | Metrics & More | Article Recommendations | Supporting Information

ABSTRACT: Amorphous polymer-derived silicon-oxycarbide (SiOC) ceramics have a high theoretical capacity and good structural stability, making them suitable anode materials for lithium-ion batteries. However, SiOC has low electronic conductivity, poor transport properties, low initial Coulombic efficiency, and limited rate capability. Therefore, there is an urgent need to explore an efficient SiOC-based anode material that could mitigate the abovementioned limitations. In this study, we synthesized carbon-rich SiOC (SiOC-I) and silicon-rich SiOC (SiOC-II) and evaluated their elemental and structural characteristics using a broad spectrum of characterization techniques. Li-ion cells were fabricated for the first time by pairing a buckypaper composed of carbon nanotubes with SiOC-I or SiOC-II as the anode. When mixed with graphene nanoplatelets, the SiOC-II/GNP composites exhibited improved electrochemical performance. High specific capacity (average specific capacity of 744 mAh/g at a 0.1C rate) was achieved with the composite anode (25 wt % SiOC-II and 75% GNP), which was much better than that of monolithic SiOC-I, SiOC-II, or GNPs. This composite also exhibited excellent cycling stability, achieving 344 mAh/g after 260 cycles at a 0.5C rate and high reversibility. The enhanced electrochemical performance is attributed to better electronic conductivity, lower charge-transfer resistance, and short ion diffusion length. Due to their superior electrochemical performance, SiOC/GNP composites with CNT buckypaper as a current collector can be considered a promising anode material for LiBs.

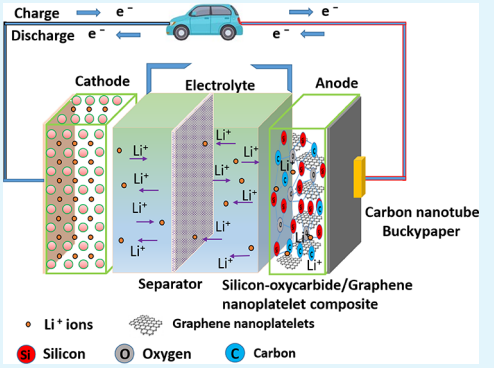

KEYWORDS: *polymer-derived ceramics, silicon-anode, buckypaper, carbon nanotubes, composites, graphene nanoplatelets, lithium-ion batteries*

Downloaded via VALDOSTA STATE UNIV on December 12, 2023 at 15:21:52 (UTC).
See https://pubs.acs.org/sharingguidelines for options on how to legitimately share published articles.

1. INTRODUCTION

The continuous usage of fossil fuels as a source of energy for more than a century has led us to global warming and other environmental issues. Therefore, global efforts are underway to generate energy via zero-emission approaches and electrifying transportation; both require high-performance energy storage systems. Li-ion batteries (LIBs) are widely used and considered the most attractive type of battery in automobiles and portable electronic devices due to their high gravimetric energy density.[1] A worldwide exploration of various anodes, cathodes, electrolytes, and current collector materials is underway to improve the performance of LIBs.[2−8] Moreover, the widespread use of portable devices and the interest in implementing small-to-medium grid storage systems have increased the demand for high-energy and long-lasting energy storage devices.[9,10] Although traditional graphite-based LIBs are available, their energy density is limited to 200 Wh/kg.[10,11] One of the current research areas in LIBs is on developing materials capable of enhancing energy and power density. The silicon anode is an excellent alternative to the existing graphite anodes because of the $Li_{22}Si_5$ storage configuration that provides an impressive charge capacity of 4200 mAh/g. However, Si as an anode material has failed to gain significant momentum due to its low electronic and ionic conductivity and significant volume expansion (~400%) upon lithiation. Si repeatedly expands and contracts during charging and discharging, leading to the crumbling and cracking of the anodes, which greatly impedes the widespread commercial use of Si-based anodes in LIBs.[12,13]

Polymer-derived silicon oxycarbide (SiOC) ceramics are an attractive alternative anode material for LIBs.[14,15] By tailoring

Received: January 18, 2023
Accepted: May 29, 2023
Published: June 13, 2023

ACS Publications

© 2023 American Chemical Society

the composition and microstructure according to end requirements, SiOC ceramics have a unique advantage in terms of their adaptability. Moreover, they possess excellent corrosion, oxidation resistance, and high thermal stability and can withstand large strains.[16−18] Notably, they can be synthesized with a micrporous structure to improve Li^+ diffusion and contain free carbon (amorphous), which acts as charge carriers.[19] Dahn *et al.* first used these materials as LIB anodes,[20] and Raj *et al.* subsequently proposed nanodomains in SiOC formed by the domain walls of SiO_2 tetrahedra surrounded by mixed SiOC bonds and an sp^2 carbon network.[21]

Fukui and coworkers created a polymer-to-ceramic microporous composite by combining and pyrolyzing polysilane with phenyl-substituted polysiloxane, $(Ph_2Si)_{0.85}(PhSi)_{0.15}$, polystyrene layers, and SiOC glasses. Furthermore, they showed that the interstitial spaces or the edges of the graphene layers serve as important electrochemically active sites for lithium storage.[19] In another study, a polysiloxane and divinylbenzene composite with phenyl substitutions was reported by Liu *et al.* at a pyrolysis temperature of 800 °C, which exhibited a stable capacity of around 660 mAh/g due to the presence of electrochemically active silicon-lithium species.[22] Nonetheless, its low electronic conductivity, large hysteresis, and high first cycle irreversibility are the key factors that limit the use of these SiOC composite anodes.

Researchers made initial attempts to fabricate carbon-enriched SiOC by mixing precursors with carbon backbone polymers, such as polystyrene,[19] acenaphthylene,[23] and divinylbenzene.[24−26] Although some of these systems have less or equal electrode capacities to commercial graphite,[24] they are more efficient than commercial graphite in promoting synergy between the carbonaceous materials for better electrochemical performance. Due to the synergistic effect between two carbonaceous materials, it is possible to improve the overall capacity of the SiOC system and cyclic stability by adding 2D carbonaceous materials. By forming a percolation network, carbonaceous materials boost the electrical conductivity of the system as well as enhance Li storage capacity and electron transfer kinetics. Numerous studies have focused on the incorporation of carbon materials into the SiOC material system, including carbon nanotubes,[27,28] graphite,[29−32] graphene nanoplatelets (GNPs),[33−38] graphene oxide,[39,40] reduced graphene oxide,[41−43] and carbon nanofibers.[44,45] Various processing methods have been employed to develop 2D carbonaceous-based SiOC anodes, like ball milling, physical mixing, sol−gel infiltration, precursor infiltration, in situ reaction, and electrospinning.[27,34−37,43,45]

However, a few recent reports on current collectors suggested that the surface roughness, structure, wettability, flexibility, compressibility, safety, and weight of the collector are important factors that need to be considered.[46,47] A typical Li-ion battery uses copper foil as the conventional metal current collector, which outweighs the overall weight of the cells. To mitigate this problem, a lightweight buckypaper made of carbon nanotubes has been identified as a current alternative collector.[48] Furthermore, with buckypaper electrodes, flexible LIBs showed no signs of cracking, delamination, or structural changes typically observed in rigid LIBs. Flexible batteries have received enormous attention recently, especially in healthcare and wearable electronics.[49] Our group previously reported[50] that due to the porous nature of buckypaper, Si nanoparticles adhere well to the buckypaper current collector upon coating. However, Si nanoparticle coating on copper foil did not adhere well as compared to buckypaper. Furthermore, SEM confirms that the bottom-most layer of Si nanoparticles is in direct contact with Cu foil or the interfacial layer. In contrast, on electrodes on buckypaper, the contact between the Si nanoparticles and the current collector is not limited to the bottom layer but is throughout the thickness. Further, using electrochemical impedance spectrocopy, our group has shown that electrodes based on buckypaper have two orders of magnitude higher diffusion constants than copper foil. Finally, it was observed that the buckypaper current collector significantly reduces the Warburg impedance and interfacial resistance between the current collector and the active material.[50]

The fabrication of SiOC anode materials using buckypaper as the current collector has not been reported in the literature. Moreover, detailed studies on SiOC graphene-based composites are still under investigation. Herein, we report the synthesis of carbon-rich SiOC and silicon-rich SiOC polymer-derived ceramics and then evaluate their structural, electronic, and electrochemical properties. Thereafter, Li-ion half-cells were fabricated with buckypaper current collectors, eliminating the use of traditional copper foil. The synthesized SiOC materials are thoroughly characterized by spectroscopic, microscopic, and electrochemical techniques prior to using them as an anode material in LIBs. This study demonstrates that the freestanding SiOC/GNP buckypaper-based electrode can be considered a good alternative anode material for LIBs. To fabricate efficient LIBs, a variety of SiOC/GNP composites were prepared by considering the synergistic effect of both SiOC and GNP, and the best-performing composite has been identified. An ideal combination of SiOC-II and GNP was achieved, which showed exceptional rate capabilities (744 mAh/g at a 0.1C rate) and good cycling stability at a higher C rate (344 mAh/g after 260 cycles at a 0.5C rate) than the monolithic SiOC-I, SiOC-II, and the pristine GNP.

2. EXPERIMENTAL SECTION

2.1. Synthesis of Carbon-Rich SiOC (SiOC-I). The precursors used to synthesize carbon-rich silicon oxycarbide ceramic (SiOC-I) were as follows: 1. linear polymethylhydrosiloxane (PHMS, $(CH_3)_3SiO[(CH_3)HSiO]_nSi(CH_3)_3$) (Sigma-Aldrich), 2. divinylbenzene (DVB, $C_6H_4(CH{=}CH_2)_2$, technical grade 80% (Sigma-Aldrich), and 3. platinum divinyltetramethyldisiloxane complex, Pt 2% in xylene (Sigma-Aldrich). The PHMS was mixed with 60% DVB and stirred at 600 rpm for 15 min followed by the addition of a 100 ppm platinum catalyst. For a homogeneous blend of the mixture, stirring continued for another 20 min. Crosslinking of the mixture was carried out in a ceramic boat for 8 h at 230 °C using a hot plate. Following crosslinking, the sample was pyrolyzed at 1000 °C for one hour with a ramp rate of 5 °C/min in an Ar atmosphere.[51]

2.2. Synthesis of Silicon-Rich SiOC (SiOC-II). A silicon-rich silicon oxycarbide glass−ceramic (SiOC-II) was synthesized using the following polymer precursors: 1. linear polymethylhydrosiloxane (PHMS, $(CH_3)_3SiO[(CH_3)HSiO]_nSi(CH_3)_3$, Sigma-Aldrich), 2. vinyl-terminated polydimethylsiloxane (PDMS, $CH_2CH[Si(CH)_2O]_nSi(CH_3)_2CHCH_2$, Sigma-Aldrich), 3. 2,4,6,8-tetramethyl-2,4,6,8-tetravinylcyclotetrasiloxane [TMTVS, $[-Si(CH_3)(CH{=}CH_2)O-]_4$, Alfa Aesar], and 4. platinum(0)-1,3-divinyl-1,1,3,3-tetramethyldisiloxane complex solution in xylene, Pt 2%, $(O[Si(CH_3)_2CH{=}CH_2]_2Pt$, Sigma-Aldrich). As a starting point, linear PHMS and TMTVS were taken in a 10:1 ratio, and PDMS was taken as 75% of the linear PHMS. After mixing, curing, and pyrolysis, the same procedure was followed as with the carbon-rich SiOC sample.[52]

https://doi.org/10.1021/acsami.3c00571
ACS Appl. Mater. Interfaces 2023, 15, 30039−30051

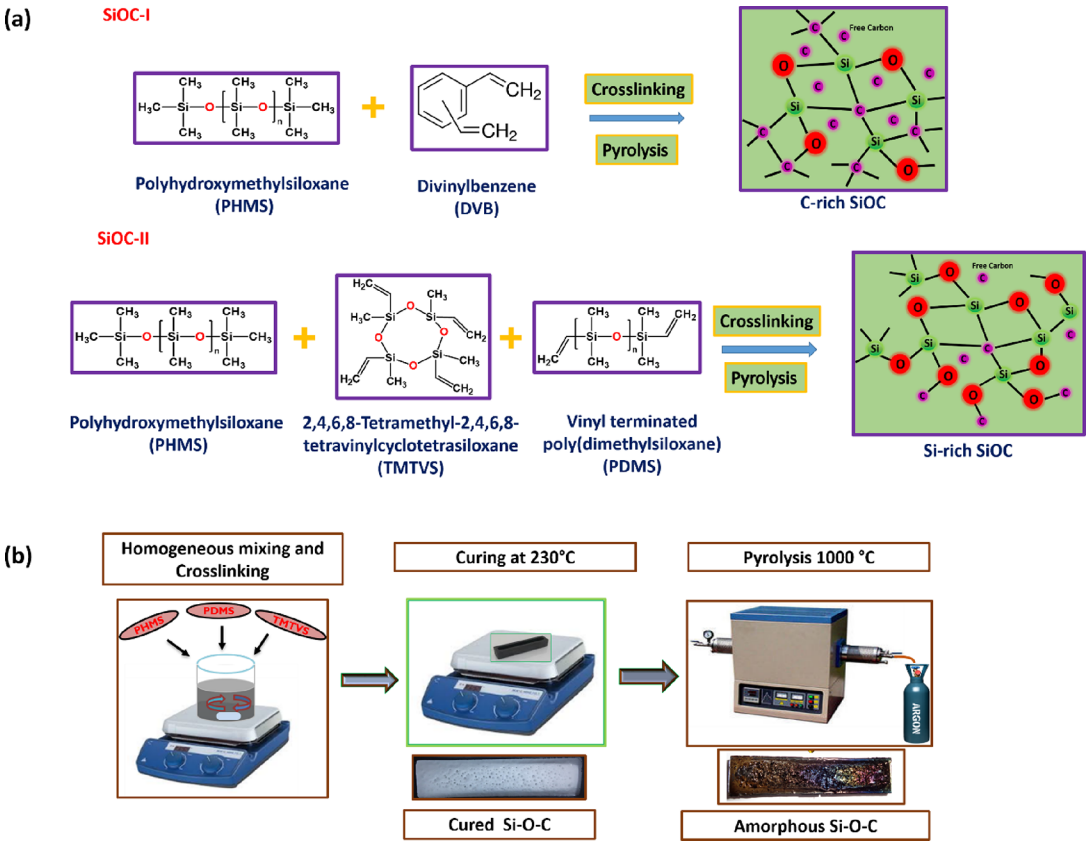

Figure 1. Schematic illustration of (a) chemical structure of carbon and silicon-rich silicon oxycarbide ceramics based on their precursors and (b) SiOC synthesis procedure.

Figure 1 shows the schematic of the synthesis process including the structure of the starting chemicals.

2.3. Chemical and Structural Characterization. Thermogravimetric analysis (TGA) [Shimadzu/DTG-60] was carried out on samples cured at 230 °C to determine the final ceramic yield. The samples were heated from room temperature to 950 °C in an argon atmosphere at a rate of 5 °C/min. To investigate the chemical structure, Fourier transform infrared (FTIR) spectroscopy was conducted on the cured and pyrolyzed SiOC-I and SiOC-II using a JASCO FTIR 4200, having a resolution of 4 cm^{-1} in the range of 4000 to 400 cm^{-1}. To confirm the amorphous nature of SiOC formed by pyrolysis at 1000 °C, X-ray diffraction (XRD) patterns were recorded using a Rigaku Ultima IV X-ray diffractometer (Cu Kα radiation, λ = 1.5418 Å, and a scan speed of 2°/min at a step size of 0.02°). Raman spectroscopy was performed using a LABRAM HR Horiba with a 100 mW Nd-YAG laser (λ = 532 nm) with a lateral resolution of 5 μm and a 30 s exposure time. Bulk elemental analysis was also carried out on ceramic samples to determine their silicon, oxygen, and carbon compositions. Leco CS744 and ONH836 analyzers were used to determine carbon and oxygen weight % in the ceramic individuals. Assuming that no other impurities are present, we estimate the balance as the weight fraction of Si. This analysis was carried out as per the reported procedure.[35,53] Additionally, to calculate the percentage and uniformity of Si, O, and C in the sample, field-emission scanning electron microscopy (FESEM) was performed using an FEI ApreoS (USA) equipped with a microanalyzer for energy-dispersive spectroscopy (EDS). The surface chemical states of the elements and their atomic and weight percentages were analyzed by X-ray photoelectron spectroscopy (XPS) [Thermo Fisher Scientific]. A monochromatic small-spot X-ray photoelectron spectrometer with a 180° double-focusing hemispherical analyzer was used with Al Kα radiation (1486.6 eV). Each element's core spectrum was scanned for 30 s and the full spectrum for 60 s. Solid-state NMR spectroscopy (Bruker ASCEND 400 MHz/54 mm long magnets, AV NEO consoles, and double-resonance 4 mm solid-state probes) was used to study ^{29}Si and ^{13}C MAS NMR. To hold the samples, a 6 mm zirconia rotor was used. Each experiment was conducted, while the sample was spinning at 10 kHz at room temperature. The ^{29}Si MAS NMR experiment was carried out with 15K transients, and the ^{13}C MAS NMR experiment was carried out with 40K transients. Cross-polarization (CP) sequences with contact times of 2.6 and 10 ms and proton decoupling were used to acquire ^{29}Si and ^{13}C NMR spectra. In both experiments, a 1 s recycle delay was used. The peaks in ^{29}Si NMR were deconvoluted and fitted using a Lorentzian fit. Finally, Brunauer–Emmett–Teller (BET BELSORP-mini II, Japan) analysis was used to determine the pyrolyzed sample specific surface area and pore volume, whereas Barrett–Joyner–Halenda (BJH) analysis was performed to determine the pore size distribution. Prior to the N_2 adsorption studies, the samples were degassed and preheated at 250 °C for 4 h. To ensure the homogeneous mixing of SiOC and GNP composites, ball milling was carried out for SiOC/GNP powders using a high-energy planetary ball mill (Pulverisette-7, Fritsch GmbH, Germany).

2.4. Preparation of Electrochemical Half-Cells. The dry powder ingredients were mixed and ball-milled for 30 min before the slurry preparation to achieve homogeneous mixing. The electrode slurry was prepared by mixing SiOC-I, SiOC-II, graphene nanoplatelet (GNP), poly(vinylidene fluoride) (PVDF, Sigma-Aldrich), and carbon Super P (MTI Corp) with a different mass ratio in *N*-methyl-2-pyrrolidone (NMP, Sigma-Aldrich). The composition, in weight percentage, of all the studied electrodes is presented in Table S1. First, PVDF was dissolved in NMP at 50 °C; then, the rest of the components were added followed by stirring for 24 h to form a castable slurry. It was then coated onto a 60 GSM buckypaper (BP, a flexible and conductive paper made of carbon nanotubes (Nanotech Lab)), using an adjustable doctor blade. To determine the active mass of the electrodes, 10 mm-diameter disks of the tape cast foils were punched, and the bare weight of the buckypaper was subtracted from

https://doi.org/10.1021/acsami.3c00571
ACS Appl. Mater. Interfaces 2023, 15, 30039−30051

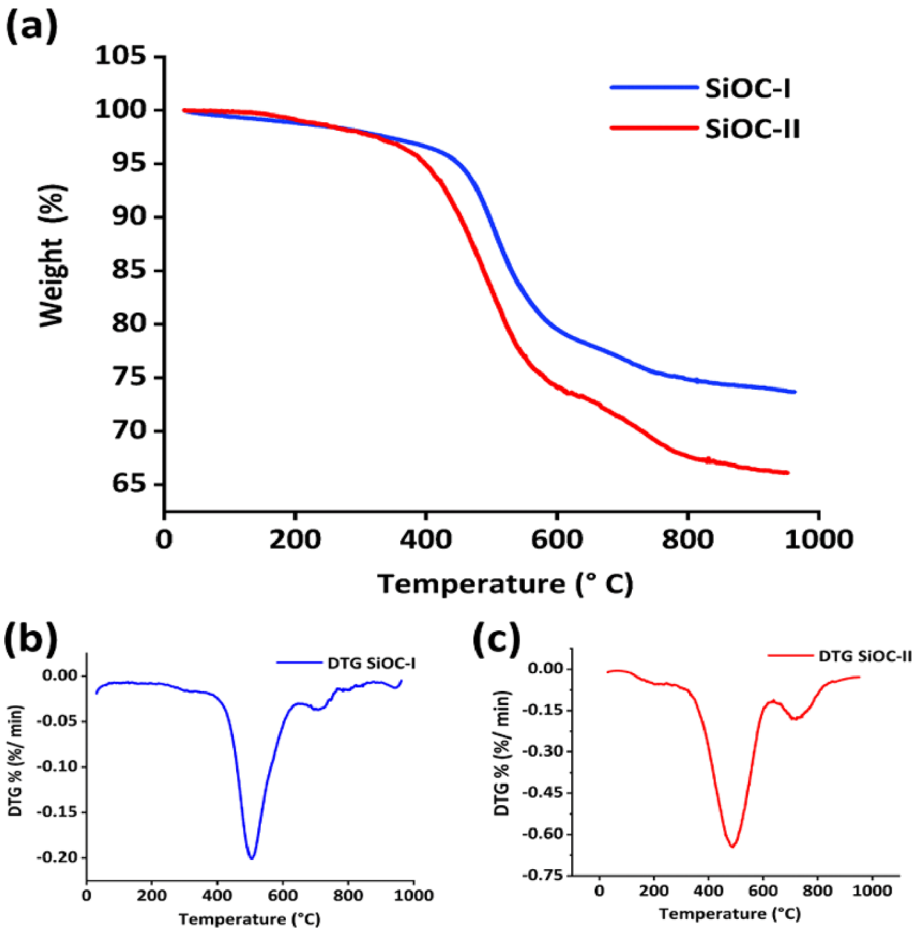

Figure 2. (a) TGA and (b,c) DTG plots of SiOC-I and SiOC-II.

the weight of the dried tape cast foils. The mass loading of the active material was in the range of 4−6 mg/cm^2. The coated samples were dried for 12 h at room temperature and another 12 h at 100 °C in a precision compact vacuum oven. Working electrodes of a diameter of 10 mm were punched. Finally, CR2032-type coin cells were assembled using MTI Corporation's Li chip as both a working electrode and a counter electrode (15.6 mm diameter × 0.45 mm thickness) for the coin cell. Lithium hexafluorophosphate ($LiPF_6$) was used as the electrolyte in ethylene carbonate and dimethyl carbonate (v/v = 1:1, Sigma-Aldrich). As the separator, Celgard 2325 (Celgard, LLC) was used. The cells were assembled in an argon glovebox and maintained at less than 0.2 ppm H_2O and O_2.

2.5. Electrochemical Studies. The galvanostatic charge−discharge cycles were conducted using a battery tester (8-channel battery analyzer, 0.005−3 A, up to 5 V, BST8-WA, MTI Corporation) with a constant-current constant-voltage (cccv) mode between 0.005 and 3 V. The first step was to test the initial capacity, and then, the rate capability was studied at different C rates (0.1, 0.5, and 1C) followed by cycling stability at a 0.1C rate (1C = 372 mA/g). The best device's cyclic stability was performed at a C rate of 0.5C. Further, the electrochemical properties of the best performing anode were determined by cyclic voltammetry (CV) at a scan rate of 0.1 mV/s using a Gamry-3000 potentiostat. Electrochemical impedance spectroscopy (EIS) was conducted at a voltage amplitude of 10 mV to measure impedances (1 MHz to 0.1 Hz at 0.005 to 3 V). Gamry Echem Analyst software was used to fit the EIS data.

3. RESULTS AND DISCUSSION

3.1. Chemical and Structural Characterization. By analyzing the thermogravimetric studies, it was concluded that SiOC-I and SiOC-II lost 26 and 34% of their weight, respectively (Figure 2a). The higher weight loss of about 8% observed in SiOC-II is due to the presence of PDMS. This PDMS acts as a sacrificial pore former and decomposes at elevated temperatures, leaving behind pores. It is also observed that the decomposition took place in two stages for both samples, as confirmed by the derivative of the TG plot (DTG) (Figure 2b,c). The first decomposition began at temperatures between 350 and 550 °C, whereas the second stage of decomposition was observed between 600 and 800 °C in both SiOC-I and SiOC-II. This two-stage decomposition is due to the reduction of silicon-containing oligomers in stage 1 and the redistribution reaction taking place due to the exchange of Si−O, Si−H, and Si−C bonds with the release of volatile compounds.[52,54,55]

FTIR spectroscopic studies of cured and pyrolyzed samples (Figure 3a,b) were conducted to examine the structural evolution of the two SiOC systems. The characteristic FTIR bands of cured precursors corresponding to 800, 900, 1020−1090, 1263, 1400, 1600, and 2963 cm^{-1} are assigned to Si−O, Si−C, Si−O−Si, Si−CH_3, CH_2═CH_2, C−H, and Si−OH, respectively. The band intensity of CH_2−CH_2 appears to be relatively higher in the cured precursor corresponding to SiOC-I, and it could be due to the addition of the carbon source DVB to the polymeric precursor.

Upon pyrolysis, the cured polymeric precursors undergo decomposition leading to the formation of bands at 1050, 1605, 2900, and 3400 cm^{-1}, which are assigned to Si−O−Si, C═C, C−H, and $Si(OH)_2$ bonds, respectively. The evaporation of CH_4 and H_2 groups from the materials during

https://doi.org/10.1021/acsami.3c00571
ACS Appl. Mater. Interfaces 2023, 15, 30039−30051

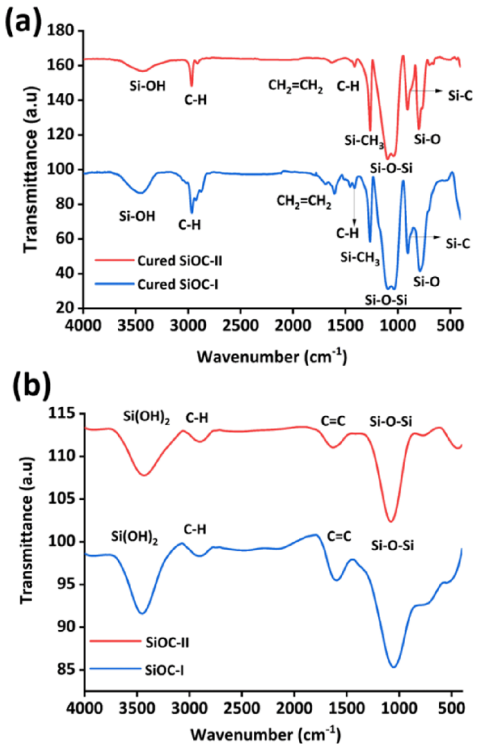

Figure 3. FTIR spectra of (a) cured precursors of SiOC-I and SiOC-II and (b) pyrolyzed SiOC-I and SiOC-II.

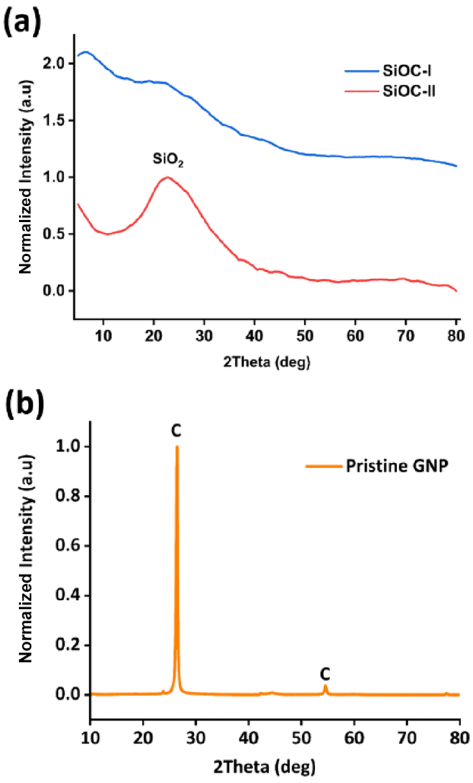

Figure 4. XRD patterns of (a) SiOC-I and SiOC-II and (b) pristine GNP.

pyrolysis accounts for the broadening of the Si−O−Si stretching bond.[52] It can be seen that both SiOC systems showed the same bands except for a variation in the band intensity at 1605 cm^{-1}, inferring the presence of more free carbon in SiOC-I. Based on the FTIR spectra of the pyrolyzed samples, it appears that there are trace amounts of hydrogen present in both the pyrolyzed samples at 1000 °C. Previous research has noted the presence of a trace amount of residual hydrogen, which is typically less than 0.3 wt %.[56,57] Hence, we have neglected the presence of hydrogen, in the pyrolyzed samples, in our study. Since FTIR did not show significant differences between the two SiOC systems; XPS, Raman, and solid-state NMR spectroscopy studies were carried out to gather further insights into the structural differences between the SiOC-I and SiOC-II.

The XRD study confirmed that both SiOC-I and SiOC-II are amorphous in nature (Figure 4a). In SiOC-II, a broad halo hump at $2\theta = 23°$ (Figure 4a) was observed and is assigned to amorphous SiO_2.[43] The diffraction peak corresponding to free carbon is absent in both SiOC-I and SiOC-II samples, suggesting that the free carbon present in both these systems is disordered. XRD of the pristine GNP (Figure 4b) displayed a sharp diffraction peak at $2\theta = 26.25°$, ascertaining the presence of crystalline carbon (JCPDS reference card 01-075-1621). Hence, it could be inferred that structural differences exist between the free carbon present in the pyrolyzed sample and externally added GNPs.

In order to ascertain the structural differences between the GNP and free carbon in these SiOC systems, Raman spectroscopy studies were performed. Three spectra were taken for each sample at different locations, and the results were identical. For carbon-rich SiOC, the disorder-induced D bands typically derived from 6-fold aromatic ring structures appear at ~1322 cm^{-1} due to the A_{1g} vibration. The G band results from in-plane bond stretching of sp^2-hybridized carbon atoms, which is observed at ~1584 cm^{-1}, as shown in Figure 5a. As a result of the background flourescence associated with

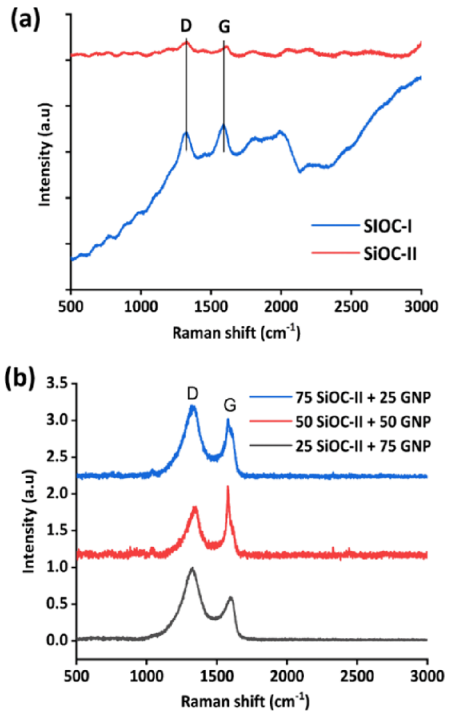

Figure 5. Raman spectra of (a) SiOC-I and SiOC-II and (b) SiOC/GNP composites with varying wt % showing the characteristic D band and G band.

https://doi.org/10.1021/acsami.3c00571
ACS Appl. Mater. Interfaces 2023, 15, 30039−30051

the amorphous nature of SiOC, the spectra recorded for the Si-rich SiOC system were noisy.[58] Even then, relatively low-intensity D and G bands were observed in SiOC II. The D band is the same for both SiOC-I and SiOC-II, but a shift of 20 cm^{-1} is observed in the G band compared to SiOC-I. In the samples, other atomic species, including Si and O, are present around the nanographitic domains, which caused the shift of the G band. Despite this, the ratio of area intensity I_D/I_G is almost the same for both the systems (Table S2). Based on the peak intensity of the D band, it can be seen that the free carbon formed is disordered. The I_D/I_G ratios reveal that both SiOC systems have more disordered carbon than the pristine GNP (Figure S1).[59] Additionally, the cluster size of graphene-like free carbon (L_a) and the point defect separation distance (L_D) in the pyrolyzed amorphous samples are calculated using the formula developed by Cançado *et al.*[60,61] and are included in eqs 1 and 2, respectively.

$$L_a = 2.4 \times 10^{-10} \times \lambda^4 \times \left(\frac{I_D}{I_G}\right)^{-1} \quad (1)$$

$$L_{2D} = 1.8 \times 10^{-9} \times \lambda^4 \times \left(\frac{I_D}{I_G}\right)^{-1} \quad (2)$$

The relatively lower L_a and L_D values for the free carbon present in SiOC systems compared to the pristine GNP confirm the disordered nature of free carbon in SiOC (Table S2). From Figure 5b, it can be inferred that when the amount of GNPs in the composite increases, the relative integrated intensity of the D band decreases and the G band increases. This can be ascertained to decrease of disorderliness of the carbon within the composite. However, no other Raman bands were observed that signify that chemical or structural changes occurred with the addition of GNPs in the SiOC-II/ GNP composites.

The elemental compositions of C, O, and Si along with the O/Si and C/Si ratios calculated using bulk elemental analysis are presented in Table S3. If any additional elements are present in the system, they will be in trace amounts and are not considered in the calculation.[62] Based on the results of the elemental analysis, SiOC-I is found to be carbon-rich, whereas SiOC-II is silicon-rich. We have also measured the elemental composition of the powdered samples by FESEM-EDX and XPS to support the results obtained from bulk elemental analysis. The elemental composition and EDX mapping of SiOC-I and SiOC-II are presented in Tables S4 and S5 and Figures S2 and S3. These studies further confirmed that SiOC-I has a carbon percentage almost twice that of SiOC-II, which is corroborated by bulk elemental analysis. The atomic and weight percentages were also measured from the surface depth profiling of XPS spectra, and the results are presented in Table S6. These results are in good agreement with that of bulk elemental analysis and FESEM-EDX. The slight variation in the weight percentages observed among XPS, EDX, and bulk elemental analysis may be due to the limitation of each technique used for the characterization.

XPS spectra were recorded to determine the types of chemical bonding and functional groups that are present on the surface of SiOC-I and SiOC-II material. The full survey scan spectra reveal the existence of C, O, and Si elements in these SiOC samples, as shown in Figure 6. The origin of the peaks is assigned based on the literature.[63] The carbon % in

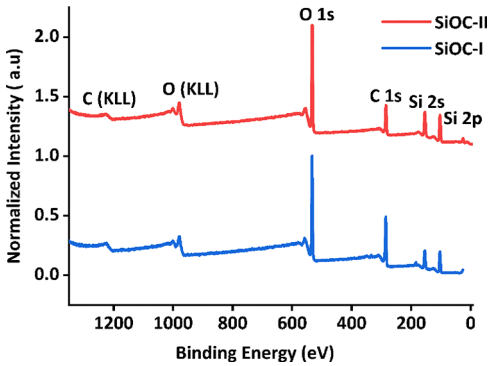

Figure 6. XPS spectra of full-range scanning for SiOC-I and SiOC-II.

SiOC-I is 50% higher (Table S6) than that of SiOC-II; this high percentage of carbon in SiOC-I could be attributed to the addition of the DVB precursor as the carbon source.

The high-resolution core-level spectra of individual elements obtained for both SiOC-I and SiOC-II samples are presented (Figure 7a–f). Upon deconvolution, the spectra unveil the different chemical bonds present among the elements. The deconvolution of C 1s spectra in Figure 7a,d implies the presence of 4 peaks at 283.95, 284.89, 286.5, and 288.9 eV and can be assigned to C–Si, C–C, C–O, and O–C═O/C═O, respectively, for both samples.[29,35] The O 1s spectra (Figure 7b,e) upon deconvolution reveal the presence of SiOC ceramic and exhibit three characteristic peaks at 531.6, 532.5, and 534.2 eV and can be assigned to C–O, Si–O, and Si–O–Si.[29,35] From the Si 2p spectra (Figure 7c) of SiOC-I, various binding states were identified, such as $SiOC_3$, SiO_3C, and SiO_4, and their binding energies are 101.2, 102.8, and 103.6 eV, respectively.[29,63,64] However, in the case of the SiOC-II sample (Figure 7f), the binding states are SiO_2C_2, SiO_3C, and SiO_4 having binding energies of 101.7, 102.8, and 103.6 eV, respectively.[29,63−66] The binding energies, various chemical states, and their atomic percentages are presented (Tables S7 and S8). The different SiOC-II/GNP composite anodes prepared on buckypaper substrates were also characterized by XPS analysis (Figure S4a–i). The various chemical states of the element within the composite remain the same as observed in individual SiOC and the pristine GNP. Moreover, the binding energy of the corresponding bond is found to be more or less the same. In contrast, the intensity of all the peaks corresponding to the carbon is increased due to the additiom of GNPs to the composite. Two additional peaks are observed in all the composites corresponding to CF (290.4 eV) and CF_2 (292.0 eV) bonds. These extra two peaks are due to the presence of the PVDF binder that was used in the preparation of the composite anode slurry.

To evaluate the nature of the bonding in the Si–O–C network, ^{29}Si MAS NMR analysis was performed for both samples (Figure S5). The deconvoluted peaks of ^{29}Si MAS NMR spectra of SiOC-I and SiOC-II are shown in Figure 8a,b. The share of the mixed-bond silicon tetrahedra (SiO_4, SiO_3C, SiO_2C_2, and $SiOC_3$) was different for the two samples, although there was no significant change in the chemical shift values (Table 1). It was observed that the SiOC-I conferred a lower amount of SiO_4 bonds (47.8%), while the silicon-rich SiOC system showed a higher amount of SiO_4 bonds (78%); this is in good agreement with the literature.[67] The C-rich SiOC-I exhibited a higher share of mixed-bond silicon tetrahedra (21.8% SiO_3C, 15.9% SiO_2C_2, and 14.5% of

https://doi.org/10.1021/acsami.3c00571
ACS Appl. Mater. Interfaces 2023, 15, 30039−30051

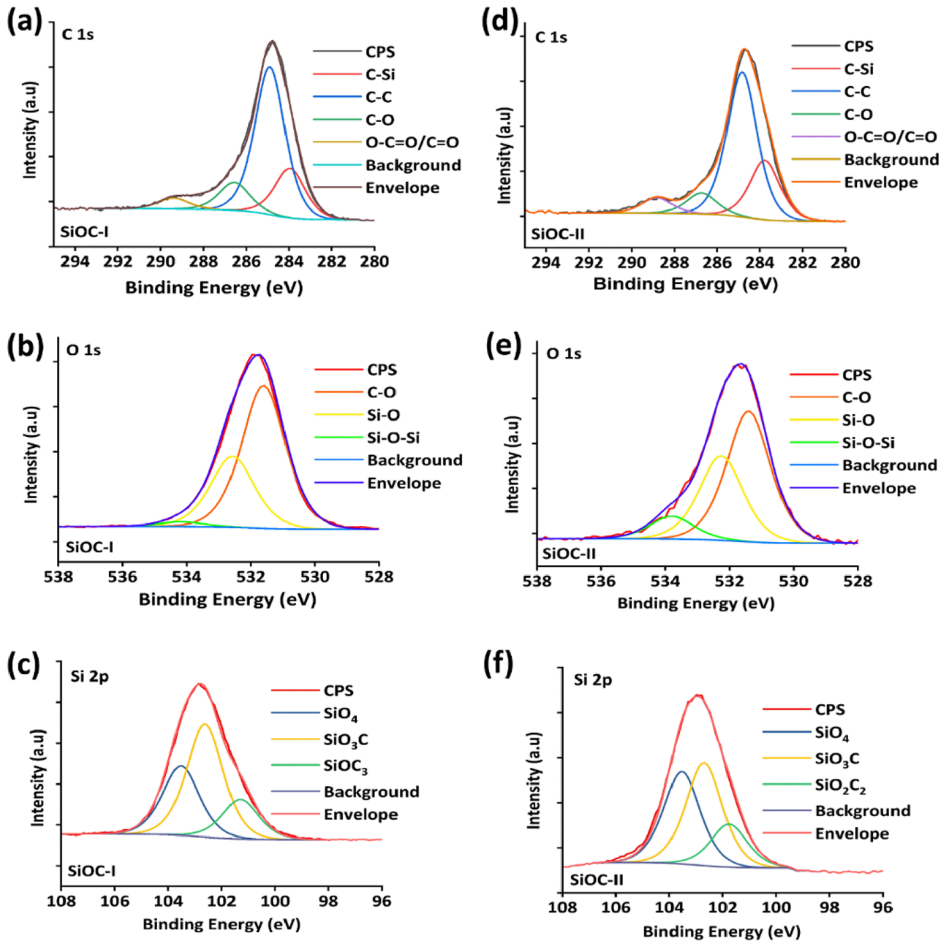

Figure 7. Deconvoluted peaks of the Si, O, and C individual XPS spectrum for SiOC-I (a–c) and SiOC-II (d–f).

$SiOC_3$). On the other hand, Si-rich SiOC-II showed a relatively lower share of mixed bonds with 19.5% SiO_3C, 2.5% SiO_2C_2, and a lack of $SiOC_3$. ^{13}C MAS NMR spectra of SiOC-I and SiOC-II are shown in Figure S6. The broad peak at ~125 ppm corresponds to the sp^2-hybridized carbon region, which is the free carbon formed in both the SiOC samples. It also revealed that during pyrolysis with PHMS and DVB in the preparation of SiOC-I, the amount of free carbon formed is more in comparison with SiOC-II. The peak ranging from 0 to −20 ppm for the SiOC-II can be assigned to aliphatic sp^3 carbon, which might have formed due to the asymmetric distribution of CH groups during pyrolysis at around 800°C.[68]

While synthesizing SiOC-II, the porosity induced by the addition of the PDMS precursor was evaluated by performing the nitrogen sorption technique. The BET specific surface area, pore volume, and mean pore diameter are presented in Table S9. It should be noted that BET analysis was carried out only for SiOC-II since pore-forming agents were added only to SiOC-II. The adsorption–desorption isotherms of SiOC-II exhibited type IV isotherms (Figure S7a), and it suggests that mesopores are present in their microstructure. From the BET studies, the specific surface area of the SiOC-II is found to be 179.3 m^2/g, and the mean pore diameter calculated from the BJH plot (Figure S7b) for SiOC-II is 2.59 nm.

3.2. Electrochemical Characterization Studies. A CR2032 coin-type half-cell was prepared by employing buckypaper as the current collector. We have used buckypaper as the current collector since there was a lack of adhesion of the ceramic particles with the Cu collector. The electrochemical performance of the individual anode materials, namely, SiOCs (SiOC-I and II) and GNPs (with and without Super P), was first evaluated using galvanostatic charge/discharge cycling at a 0.1C rate (1C = 372 mAh/g). Figure 9a shows the initial charge/discharge curves of different anode materials. Among the two SiOC anode materials tested, SiOC-II delivered a high initial discharge capacity of 1337 mAh/g and a charge capacity of 788 mAh/g with an initial Coulombic efficiency (ICE) of 58.9%, whereas SiOC I delivered a good initial discharge capacity of 1113 mAh/g but a low charge capacity of 414 mAh/g, giving an ICE of 37.1%. The initial irreversible capacity loss in both SiOC systems can be mainly attributed to the formation of the SEI layer, electrolyte decomposition on the surface, and side reactions. The SEI layer results in irreversible first-cycle capacity leading to a lower ICE value, which is similar to ICE values reported by another group.[38] The high first-cycle irreversibility of SiOC-I can be attributed to the presence of the irreversible nature of $SiOC_3$ units that disappear upon initial cycling, whereas the absence of the $SiOC_3$ phase in SiOC-II might have led to the improved reversible capacity (Table 1). Further, the presence of SiO_4, SiO_3C, and SiO_2C_2 tetrahedral silica species in SiOC-II could have been attributed to its reversible lithium insertion.[22] Although SiOCs are inherently porous, the higher specific surface area (179.3 m^2/g) (Table S9) of SiOC-II achieved by adding PDMS would have efficiently accommodated the volume expansion during the lithiation. This

https://doi.org/10.1021/acsami.3c00571
ACS Appl. Mater. Interfaces 2023, 15, 30039–30051

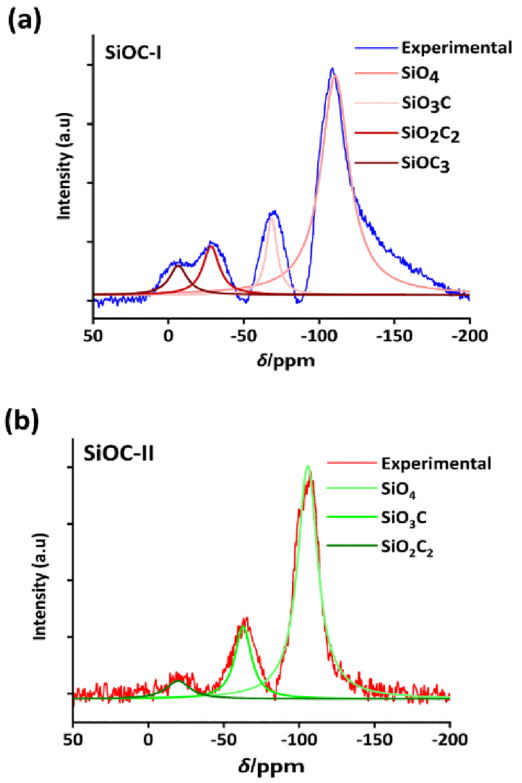

Figure 8. Deconvoluted peaks of ^{29}Si MAS NMR spectra of (a) SiOC-I and (b) SiOC-II samples.

might be the reason for the structural stability of SiOC-II leading to large reversible capacity. Although it is ascertained that an increase in the free carbon domain would lead to improved storage capacities,[19,22] it was difficult to correlate it in our studies due to the diverse microstructures exhibited by the PDCs. Moreover, at the 10th cycle, SiOC-I shows a discharge/charge capacity of 376/352 mAh/g with a Coulombic efficiency of 93.6%; similarly, SiOC-II shows a discharge/charge capacity of 693/677 mAh/g with a Coulombic efficiency of 97.6%. These high Coulombic efficiencies signify that the system is structurally stable.

As a control experiment, galvanostatic charge/discharge tests for the GNP material system were performed with and without the addition of carbon black (Super P). The anodes made of GNPs (with and without the addition of Super P) demonstrated the initial discharge capacities of 1003 and 859 mAh/g and corresponding charge capacities of 634 and 592 mAh/g, with ICE values of 63.2 and 68.9%, respectively (Figure 9a). At the 10th cycle, both the GNP systems showed a stable discharge and charge capacity of 647/632 mAh/g and 598/580 mAh/g with Coulombic efficiencies of 97.6 and 96.9%, respectively. The results obtained for the GNP system are in good agreement with the previous study.[69] The lower capacity values of the GNP system without the addition of Super P may be because of the effect of the PVDF binder that acts as an insulating site in the electrode leading to a reduction in the lithiation kinetics.

Since SiOC-II exhibited better electrochemical performance compared to SiOC-I, composite anodes were prepared by adding varying weight fractions of GNPs to SiOC-II. The galvanostatic charge−discharge tests were conducted under similar conditions as considered earlier. The three composite anodes, namely, 75 SiOC-II + 25 GNP, 50 SiOC-II + 50 GNP, and 25 SiOC-II + 75 GNP, delivered the initial discharge capacities of 1030, 1026, and 1204 mAh/g, and the corresponding charge capacities are 561, 583, and 744 mAh/g as shown in Figure 9a. The ICE values of these composites are 54.4, 55.7, and 61.7%, respectively. At the 10th cycle, composites demonstrated stable discharge/charge capacities of 414/411, 526/526, and 726/692 mAh/g with Coulombic efficiencies of 99.2, 100, and 95.3%, respectively. The exceptional Coulombic efficiencies exhibited by the composite systems can be attributed to the improved structural stability and the formation of a highly conductive electrically percolating network of GNPs in the SiOC-II matrix.[70] Further, the porous network of amorphous SiOC-II facilitates the liquid electrolyte to penetrate to the interior of the electrode and provides unobstructed pathways for Li-ion transport, reducing the diffusion lengths as well as exposing more active sites.[71] Due to its high conductivity and robust nature, the buckypaper used here as a current collector is postulated to offer very low internal contact resistance between the anode and the current collector, leading to efficient electron transport upon lithiation and delithiation.[72]

The rate capability of all the electrodes was evaluated and compared. The specific capacities at different current rates (0.1, 0.5, and 1C rate) are shown in Figure 9b. It is obvious that with the increase in the current rates, the specific capacity of the system decreases because of mechanically induced damage of active particles, which would lead to an increase in the internal resistance. In the case of 25 SiOC-II + 75 GNP electrodes, specific capacities of 744, 592, and 472 mAh/g were obtained at 0.1, 0.5, and 1C, respectively. The specific capacities obtained for the 25 SiOC-II + 75 GNP electrodes were found to be the best among all the electrodes investigated in this study and other studied graphite anodes.

Table 2 displays the initial charge−discharge capacity, initial Coulombic efficiency, average discharge-specific capacities at different C rates (0.1, 0.5, and 1C), and specific capacity retention after 35 cycles. The rate capability studies indicate that capacity was almost fully recovered in all compositions when the current was switched back to 0.1C, indicating that high-rate cycling was not damaging to the structure of the electrode materials. A nearly 100% Coulombic efficiency was seen with all electrodes up to 35 cycles, demonstrating stable electrochemical reactions.

The CV plot (Figure S8) shows four cycles of voltammograms for 25 SiOC-II + 75 GNP at a scan rate of 0.1 mV s^{-1}

Table 1. Data Representing the Various Bonds and Their Percentage Were Identified from the Deconvolution of ^{29}Si MAS NMR Spectra of SiOC-I and SiOC-II Samples

	SiO_4		SiO_3C		SiO_2C_2		$SiOC_3$	
material	δ/ppm	%	δ/ppm	%	δ/ppm	%	δ/ppm	%
SiOC-I	−101.5	47.8	−64.8	21.8	−27.6	15.9	−1.7	14.5
SiOC-II	−107.6	78.0	−65.4	19.5	−28.6	2.5		

https://doi.org/10.1021/acsami.3c00571
ACS Appl. Mater. Interfaces 2023, 15, 30039−30051

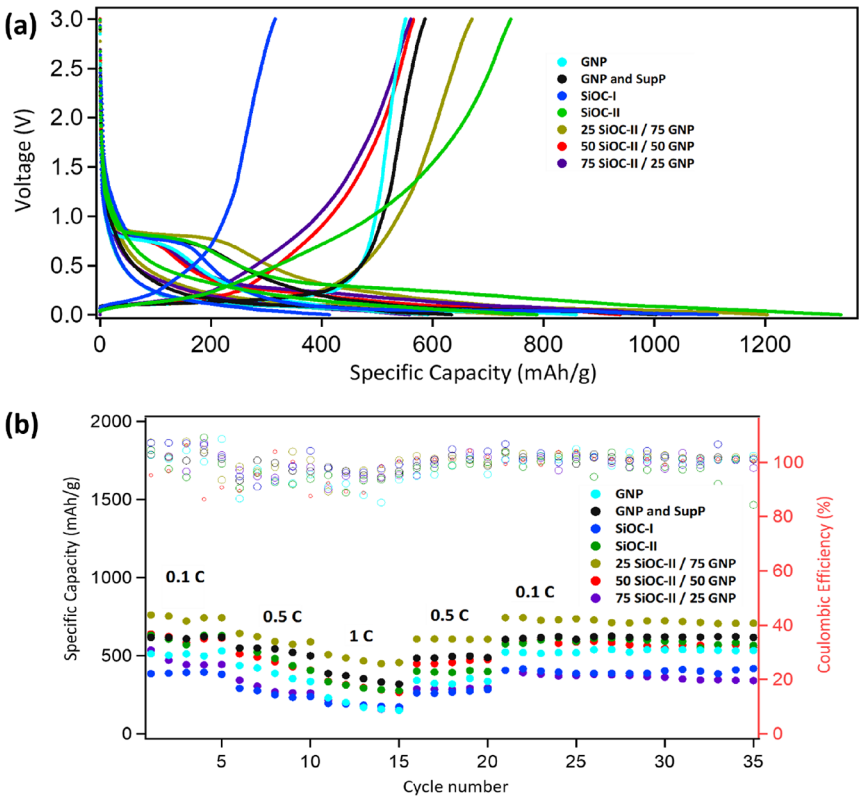

Figure 9. (a) Initial discharge/charge capacity of GNPs, SiOC-I, and SiOC-II and their composites at 0.1C. (b) Plot showing the rate capability of various anode materials at 0.1, 0.5, and 1C rates.

Table 2. First-Cycle Discharge/Charge Capacity, Initial Coulombic Efficiency, Average Discharge Capacities at Different C Rates, and Capacity Retention after 35 Cycles

anode material	initial cycle discharge capacity (mAh/g)	initial cycle charge capacity (mAh/g)	initial Coulombic efficiency (η) %	average specific capacity of 5 cycles (mAh/g)	average specific capacity of 5 cycles (0.5C rate) (mAh/g)	average specific capacity of 5 cycles (1C rate) (mAh/g)	cyclic stability after 35 cycles (0.1C rate) (mAh/g)
GNP	859	592	68.9	582	386	202	530
GNP and Super P	1003	634	63.2	651	533	352	618
SiOC-I	1113	414	37.1	388	255	183	402
SiOC-II	1337	788	58.9	738	480	300	585
75SiOC-II/ 25GNP	1030	561	54.4	482	270	180	352
50SiOC-II/ 50GNP	1046	583	55.7	550	462	317	536
25SiOC-II/ 75GNP	1204	744	61.79	728	592	472	688

for a voltage range of 0.005−3.0 V. The peak at 0.58 V in the cathodic scan is attributed to the decomposition of electrolytes at the electrode surface. Peaks at 0.005 and 0.32 V are attributed to the insertion and extraction of Li^+ ions in SiOC-II, respectively. Moreover, the CV curves for the composite electrodes of 25 SiOC-II + 75 GNP overlapped from the second to fourth cycle, suggesting excellent reversibility of lithiation and delithiation. The galvanostatic charge−discharge profiles of the 25 SiOC-II + 75 GNP electrodes for the 1st, 5th, 10th, 15th, 20th, and 40th cycles at 0.1C are displayed in Figure 10a. The Coulombic efficiency is nearly 100% for all the cycles showing good cycling stability. At all C rates, the 25 SiOC-II + 75 GNP electrode exhibited the highest specific capacity.

Finally, the best-performing 25 SiOC-II + 75 GNP anode has been characterized by its cyclic stability. At 0.5C, the initial discharge-specific capacity of 25 SiOC-II + 75 GNP electrodes is 374 mAh/g, and after 260 cycles, it maintains a reversible capacity of 344 mAh/g (Figure S9). The increase in discharge capacity in the intermediate stage of the test may be accounted for by the dense surface and large average particle size, which might prolong the activation process. Furthermore, direct contact between SiOC-II and the electrolyte results in the decomposition of the electrolyte, which leads to some capacity

https://doi.org/10.1021/acsami.3c00571
ACS Appl. Mater. Interfaces 2023, 15, 30039−30051

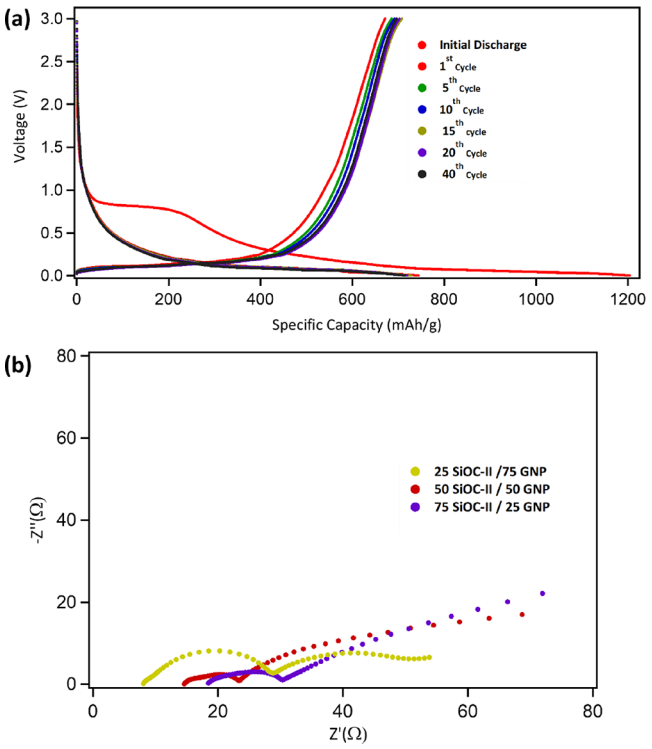

Figure 10. (a) Galvanostatic charge−discharge profile of the 25 SiOC-II/75 GNP composite at the 1st, 5th, 10th, 15th, 20th, and 40th cycle. (b) Comparison of EIS data of all 3 SiOC/GNP composite samples at the 10th cycle.

loss with the increasing number of cycles, and this phenomenon has also been reported.[38,73]

To gain insights into the Li-ion storage of the SiOC/GNP composites, electrochemical impedance spectroscopic (EIS) characterization was performed to determine equivalent circuit diagrams. The Nyquist plot and equivalent circuit are shown in the Supporting Information (Figure S10). For the composite electrodes, EIS measurements were recorded at the end of the 1st, 4th, 7th, and 10th cycles (i.e., discharged to 0.005 V), and Nyquist plots are presented in Figure S11a−c. It is evident from Figure S11a that the 25 SiOC-II + 75 GNP composite has the smallest semicircle diameter, indicating that it has the lowest contact and charge transfer resistance (R_{ct}).

According to the EIS results, the total resistance decreases from the 1st cycle to the 10th cycle. In all cycles, the 25 SiOC-II + 75 GNP electrode showed a lower series resistance than the others. The series resistance values of 19, 15, and 8 Ω are measured for 75 SiOC-II + 25 GNP, 50 SiOC-II + 50 GNP, and 25 SiOC-II + 75 GNP electrodes, respectively, in the 10th cycle (Figure 10b). A lower series resistance corresponds to a higher specific capacity value, i.e., the 25 SiOC-II + 75 GNP electrode, with the lowest series resistance leading to the highest specific capacity at all C rates. The porosity present in the SiOC-II might have improved the kinetics of Li-ion transport, which led to the improved reversible capacity in SiOC-II.[65] The highly conducting buckypaper current collector helps in the fast transfer of electrons when the Li ions intercalate and deintercalate during cycling.

4. CONCLUSIONS

In this article, we synthesized carbon-rich and silicon-rich SiOC ceramics and characterized them using various spectroscopic (FTIR, Raman, XRD, XPS, and solid-state NMR), microscopic (FESEM-EDX), thermogravimetric (TGA/DTG), and bulk elemental (CHNO) techniques. Electrodes were made using carbon- and silicon-rich SiOC ceramics and their composites with graphene nanoplatelets (GNPs). This is the first time that buckypaper has been successfully used as a current collector for SiOC anodes. The best electrochemical performance was achieved by a SiOC/GNP composite anode composed of Si-rich SiOC. Compared to monolithic SiOC-I, SiOC-II, and GNPs, a SiOC-II/GNP composite containing 25 wt % SiOC-II and 75 wt % GNP demonstrated superior battery performance (average specific capacity of ∼744 mAh/g at a 0.1C rate) and stability. In addition to a reduced charge-transfer resistance, low ion diffusion distance, and less agglomeration, better electronic conductivity contributed to an enhanced specific capacity. After 35 cycles at a 0.1C rate, 25 SiOC-II + 75 GNP demonstrates excellent cycling stability, achieving 688 mAh/g and high reversibility. At a 0.5C rate, the initial capacity is 374 mAh/g, and after 260 cycles, it maintains a reversible capacity of 344 mAh/g. In this study, composite electrodes and buckypaper to serve as a current collector provide a new direction for developing highly efficient LIBs.

■ ASSOCIATED CONTENT

Supporting Information

The Supporting Information is available free of charge at https://pubs.acs.org/doi/10.1021/acsami.3c00571.

Data plots and tables corresponding to slurry ratios for cell fabrication, Raman plot of pristine GNP and data of various parameters, elemental analysis from CHNO analysis, FESEM-EDX mapping, XPS, ^{29}Si and ^{13}C NMR of SiOC and SiOC-II ceramic, XPS spectrum of SiOC/GNP composites, cyclic voltametry, cyclic stability of 25% SiOC + 75% GNP, and EIS studies on all other SiOC/GNP composites (PDF)

■ AUTHOR INFORMATION

Corresponding Author

Rajendra K. Bordia − *Department of Materials Science and Engineering, Clemson University, Clemson, South Carolina 29634, United States;* orcid.org/0000-0001-9256-0301; Email: rbordia@clemson.edu

Authors

Gangadhar Jella − *Mechanical Engineering Department, Birla Institute of Technology and Science Pilani-Hyderabad Campus, Hyderabad, Telangana 500078, India; Materials Centre for Sustainable Energy and Environment, Birla Institute of Technology and Science Pilani-Hyderabad Campus, Hyderabad, Telangana 500078, India*

Dillip K. Panda − *Department of Materials Science and Engineering, Clemson University, Clemson, South Carolina 29634, United States*

Nawraj Sapkota − *Department of Physics and Astronomy, Clemson Nanomaterials Institute, Clemson University, Clemson, South Carolina 29634, United States*

Michelle Greenough − *Department of Materials Science and Engineering, Clemson University, Clemson, South Carolina 29634, United States;* orcid.org/0000-0002-3016-7886

Santanu P. Datta − *Mechanical Engineering Department, Birla Institute of Technology and Science Pilani-Hyderabad*

https://doi.org/10.1021/acsami.3c00571
ACS Appl. Mater. Interfaces 2023, 15, 30039−30051

Campus, Hyderabad, Telangana 500078, India; Materials Centre for Sustainable Energy and Environment, Birla Institute of Technology and Science Pilani-Hyderabad Campus, Hyderabad, Telangana 500078, India

Apparao M. Rao − *Department of Physics and Astronomy, Clemson Nanomaterials Institute, Clemson University, Clemson, South Carolina 29634, United States;* orcid.org/0000-0002-1450-3499

Ravindran Sujith − *Mechanical Engineering Department, Birla Institute of Technology and Science Pilani-Hyderabad Campus, Hyderabad, Telangana 500078, India; Materials Centre for Sustainable Energy and Environment, Birla Institute of Technology and Science Pilani-Hyderabad Campus, Hyderabad, Telangana 500078, India;* orcid.org/0000-0003-0835-4471

Complete contact information is available at: https://pubs.acs.org/10.1021/acsami.3c00571

Author Contributions

⊥G.J. and D.K.P. contributed equally to this paper.

Notes

The authors declare no competing financial interest.

■ ACKNOWLEDGMENTS

The authors would like to acknowledge the Central Analytical Laboratory (CAL) facility at the BITS-Pilani Hyderabad campus for giving access to facilities such as FTIR, TGA, XRD, XPS, FESEM-EDX, and solid-state NMR. We also acknowledge the Central Sophisticated Instrumentation Facility (CSIF) of the BITS-Pilani Goa campus for the Raman spectroscopy facility. We thank the Sophisticated Analytical Instrumentation Facility (SAIF) at IIT Madras for conducting bulk elemental analysis using a CHNO analyzer. We appreciate the extended support provided by (i) Dr. Krishna Gopal Maiti, Research Scientist at Genomics Research Center in Academia Sinica, Taiwan, regarding the discussions on solid-state NMR characterization, and (ii) Dr. Kelliann Koehler of the Clemson EM lab for her XPS expertise. This work was partly supported by the US National Science Foundation EPSCoR Program under NSF award no. OIA-1655740. Additional support from the US National Science Foundation Graduate Research Fellowship Program GRFP (DGE-1744593) for M.G. is also acknowledged. However, opinions, findings, and conclusions or recommendations expressed in this material are those of the authors and do not necessarily reflect those of the US National Science Foundation.

■ REFERENCES

(1) Nitta, N.; Wu, F.; Lee, J. T.; Yushin, G. Li-Ion Battery Materials: Present and Future. *Mater. Today* **2015**, *18*, 252−264.

(2) Azami-Ghadkolai, M.; Yousefi, M.; Allu, S.; Creager, S.; Bordia, R. Effect of Isotropic and Anisotropic Porous Microstructure on Electrochemical Performance of Li Ion Battery Cathodes: An Experimental and Computational Study. *J. Power Sources* **2020**, *474*, No. 228490.

(3) Ghadkolai, M. A.; Creager, S.; Nanda, J.; Bordia, R. K. Freeze Tape Cast Thick Mo Doped Li4Ti5O12 Electrodes for Lithium-Ion Batteries. *J. Electrochem. Soc.* **2017**, *164*, A2603.

(4) Ventrapragada, L. K.; Creager, S. E.; Rao, A. M.; Podila, R. Carbon Nanotubes Coated Paper as Current Collectors for Secondary Li-Ion Batteries. *Nanotechnol. Rev.* **2019**, *8*, 18−23.

(5) Ventrapragada, L. K.; Zhu, J.; Creager, S. E.; Rao, A. M.; Podila, R. A Versatile Carbon Nanotube-Based Scalable Approach for Improving Interfaces in Li-Ion Battery Electrodes. *ACS Omega* **2018**, *3*, 4502−4508.

(6) Liang, F.; Wu, D.; Jiang, L.; Zhang, Z.; Zhang, W.; Rui, Y.; Tang, B.; Liu, F. Layered Niobium Oxide Hydrate Anode with Excellent Performance for Lithium-Ion Batteries. *ACS Appl. Mater. Interfaces* **2021**, *13*, 51057−51065.

(7) Liu, Y.; Li, W.; Xia, Y. Recent Progress in Polyanionic Anode Materials for Li (Na)-Ion Batteries. *Electrochem. Energ. Rev.* **2021**, *4*, 447−472.

(8) Wang, J.; Wang, Z.; Ni, J.; Li, L. Electrospun Materials for Batteries Moving Beyond Lithium-Ion Technologies. *Electrochem. Energy Rev.* **2022**, *5*, 211−241.

(9) Nishi, Y. Lithium Ion Secondary Batteries; Past 10 Years and the Future. *J. Power Sources* **2001**, *100*, 101−106.

(10) Tarascon, J.-M.; Armand, M. Issues and Challenges Facing Rechargeable Lithium Batteries. *Nature* **2001**, *414*, 359−367.

(11) Asenbauer, J.; Eisenmann, T.; Kuenzel, M.; Kazzazi, A.; Chen, Z.; Bresser, D. The Success Story of Graphite as a Lithium-Ion Anode Material − Fundamentals, Remaining Challenges, and Recent Developments Including Silicon (Oxide) Composites. *Sustainable Energy Fuels* **2020**, *4*, 5387−5416.

(12) Zhang, C.; Wang, F.; Han, J.; Bai, S.; Tan, J.; Liu, J.; Li, F. Challenges and Recent Progress on Silicon-Based Anode Materials for Next-Generation Lithium-Ion Batteries. *Small Structures* **2021**, *2*, 2100009.

(13) Luo, W.; Chen, X.; Xia, Y.; Chen, M.; Wang, L.; Wang, Q.; Li, W.; Yang, J. Surface and Interface Engineering of Silicon-Based Anode Materials for Lithium-Ion Batteries. *Adv. Energy Mater.* **2017**, *7*, 1701083.

(14) Wen, Q.; Qu, F.; Yu, Z.; Graczyk-Zajac, M.; Xiong, X.; Riedel, R. Si-Based Polymer-Derived Ceramics for Energy Conversion and Storage. *J Adv Ceram* **2022**, *11*, 197−246.

(15) Mukherjee, S.; Ren, Z.; Singh, G. Molecular Polymer-Derived Ceramics for Applications in Electrochemical Energy Storage Devices. *J. Phys. D: Appl. Phys.* **2018**, *51*, 463001.

(16) Sujith, R.; Jothi, S.; Zimmermann, A.; Aldinger, F.; Kumar, R. Mechanical Behaviour of Polymer Derived Ceramics − a Review. *Int. Mater. Rev.* **2021**, *66*, 426−449.

(17) Barroso, G.; Li, Q.; Bordia, R. K.; Motz, G. Polymeric and Ceramic Silicon-Based Coatings − a Review. *J. Mater. Chem. A* **2019**, *7*, 1936−1963.

(18) Stabler, C.; Ionescu, E.; Graczyk-Zajac, M.; Gonzalo-Juan, I.; Riedel, R. Silicon Oxycarbide Glasses and Glass-Ceramics: "All-Rounder" Materials for Advanced Structural and Functional Applications. *J. Am. Ceram. Soc.* **2018**, *101*, 4817−4856.

(19) Fukui, H.; Ohsuka, H.; Hino, T.; Kanamura, K. A Si−O−C Composite Anode: High Capability and Proposed Mechanism of Lithium Storage Associated with Microstructural Characteristics. *ACS Appl. Mater. Interfaces* **2010**, *2*, 998−1008.

(20) Wilson, A. M.; Xing, W.; Zank, G.; Yates, B.; Dahn, J. R. Pyrolysed Pitch-Polysilane Blends for Use as Anode Materials in Lithium Ion Batteries II: The Effect of Oxygen. *Solid State Ionics* **1997**, *100*, 259−266.

(21) Saha, A.; Raj, R.; Williamson, D. L. A Model for the Nanodomains in Polymer-Derived SiCO. *J. Am. Ceram. Soc.* **2006**, *0*, 2188.

(22) Liu, X.; Zheng, M.-C.; Xie, K. Mechanism of Lithium Storage in Si−O−C Composite Anodes. *J. Power Sources* **2011**, *196*, 10667−10672.

(23) Fukui, H.; Ohsuka, H.; Hino, T.; Kanamura, K. Polysilane/Acenaphthylene Blends Toward Si−O−C Composite Anodes for Rechargeable Lithium-Ion Batteries. *J. Electrochem. Soc.* **2011**, *158*, A550.

(24) Dibandjo, P.; Graczyk-Zajac, M.; Riedel, R.; Pradeep, V. S.; Soraru, G. D. Lithium Insertion into Dense and Porous Carbon-Rich Polymer-Derived SiOC Ceramics. *J. Eur. Ceram. Soc.* **2012**, *32*, 2495−2503.

(25) Graczyk-Zajac, M.; Vrankovic, D.; Waleska, P.; Hess, C.; Sasikumar, P. V.; Lauterbach, S.; Kleebe, H.-J.; Sorarú, G. D. The Li-Storage Capacity of SiOC Glasses with and without Mixed Silicon Oxycarbide Bonds. *J. Mater. Chem. A* **2018**, *6*, 93−103.
(26) Liu, G.; Kaspar, J.; Reinold, L. M.; Graczyk-Zajac, M.; Riedel, R. Electrochemical Performance of DVB-Modified SiOC and SiCN Polymer-Derived Negative Electrodes for Lithium-Ion Batteries. *Electrochim. Acta* **2013**, *106*, 101−108.
(27) Shen, J.; Ahn, D.; Raj, R. C-Rate Performance of Silicon Oxycarbide Anodes for Li+ Batteries Enhanced by Carbon Nanotubes. *J. Power Sources* **2011**, *196*, 2875−2878.
(28) Bhandavat, R.; Singh, G. Stable and Efficient Li-Ion Battery Anodes Prepared from Polymer-Derived Silicon Oxycarbide−Carbon Nanotube Shell/Core Composites. *J. Phys. Chem. C* **2013**, *117*, 11899−11905.
(29) Wu, Z.; Cheng, X.; Tian, D.; Gao, T.; He, W.; Yang, C. SiOC Nanolayers Directly-Embedded in Graphite as Stable Anode for High-Rate Lithium Ion Batteries. *Chem. Eng. J.* **2019**, *375*, No. 121997.
(30) Knozowski, D.; Graczyk-Zając, M.; Vrankovic, D.; Trykowski, G.; Sawczak, M.; De Carolis, D. M.; Wilamowska-Zawłocka, M. New Insights on Lithium Storage in Silicon Oxycarbide/Carbon Composites: Impact of Microstructure on Electrochemical Properties. *Composites, Part B* **2021**, *225*, No. 109302.
(31) Saleh, I.; Raj, R. Three-Dimensional Architecture of Lithium-Anodes Made from Graphite Fibers Coated with Thin-Films of Silicon Oxycarbide: Design, Performance and Manufacturability. *J. Power Sources* **2016**, *310*, 18−25.
(32) Knozowski, D.; Graczyk-Zajac, M.; Trykowski, G.; Wilamowska-Zawłocka, M. Silicon Oxycarbide-Graphite Electrodes for High-Power Energy Storage Devices. *Materials* **2020**, *13*, 4302.
(33) Ji, F.; Li, Y.-L.; Feng, J.-M.; Su, D.; Wen, Y.-Y.; Feng, Y.; Hou, F. Electrochemical Performance of Graphene Nanosheets and Ceramic Composites as Anodes for Lithium Batteries. *J. Mater. Chem.* **2009**, *19*, 9063.
(34) Ren, Y.; Yang, B.; Huang, X.; Chu, F.; Qiu, J.; Ding, J. Intercalated SiOC/Graphene Composites as Anode Material for Li-Ion Batteries. *Solid State Ionics* **2015**, *278*, 198−202.
(35) David, L.; Bhandavat, R.; Barrera, U.; Singh, G. Silicon Oxycarbide Glass-Graphene Composite Paper Electrode for Long-Cycle Lithium-Ion Batteries. *Nat. Commun.* **2016**, *7*, 10998.
(36) Sang, Z.; Zhao, Z.; Su, D.; Miao, P.; Zhang, F.; Ji, H.; Yan, X. SiOC Nanolayer Wrapped 3D Interconnected Graphene Sponge as a High-Performance Anode for Lithium Ion Batteries. *J. Mater. Chem. A* **2018**, *6*, 9064−9073.
(37) Sang, Z.; Yan, X.; Wen, L.; Su, D.; Zhao, Z.; Liu, Y.; Ji, H.; Liang, J.; Dou, S. X. A Graphene-Modified Flexible SiOC Ceramic Cloth for High-Performance Lithium Storage. *Energy Storage Materials* **2020**, *25*, 876−884.
(38) Shao, G.; Hanaor, D. A. H.; Wang, J.; Kober, D.; Li, S.; Wang, X.; Shen, X.; Bekheet, M. F.; Gurlo, A. Polymer-Derived SiOC Integrated with a Graphene Aerogel As a Highly Stable Li-Ion Battery Anode. *ACS Appl. Mater. Interfaces* **2020**, *12*, 46045−46056.
(39) Zhang, Z.; Calderon, J. E.; Fahad, S.; Ju, L.; Antony, D.-X.; Yang, Y.; Kushima, A.; Zhai, L. Polymer-Derived Ceramic Nanoparticle/Edge-Functionalized Graphene Oxide Composites for Lithium-Ion Storage. *ACS Appl. Mater. Interfaces* **2021**, *13*, 9794−9803.
(40) Kolathodi, M. S.; David, L.; Abass, M. A.; Singh, G. Polysiloxane-Functionalized Graphene Oxide Paper: Pyrolysis and Performance as a Li-Ion Battery and Supercapacitor Electrode. *RSC Adv.* **2016**, *6*, 74323−74331.
(41) David, L.; Shareef, K. M.; Abass, M. A.; Singh, G. Three-Dimensional Polymer-Derived Ceramic/Graphene Paper as a Li-Ion Battery and Supercapacitor Electrode. *RSC Adv.* **2016**, *6*, 53894−53902.
(42) Islam, M. S.; Karim, M. R.; Islam, S.; Kim, J.; Rabin, N. N.; Ohtani, R.; Nakamura, M.; Koinuma, M.; Hayami, S. S.; Karim, M. R.; Islam, S.; Kim, J.; Rabin, N. N.; Ohtani, R.; Nakamura, M.; Koinuma, M.; Hayami, S. *In Situ* Generation of Silicon Oxycarbide Phases on Reduced Graphene Oxide for Li-Ion Battery Anode. *ChemistrySelect* **2016**, *1*, 6429−6433.
(43) Ma, M.; Wang, H.; Xiong, L.; Huang, S.; Li, X.; Du, X. Self-Assembled Homogeneous SiOC@C/Graphene with Three-Dimensional Lamellar Structure Enabling Improved Capacity and Rate Performances for Lithium Ion Storage. *Carbon* **2022**, *186*, 273−281.
(44) Li, Y.; Hu, Y.; Lu, Y.; Zhang, S.; Xu, G.; Fu, K.; Li, S.; Chen, C.; Zhou, L.; Xia, X.; Zhang, X. One-Dimensional SiOC/C Composite Nanofibers as Binder-Free Anodes for Lithium-Ion Batteries. *J. Power Sources* **2014**, *254*, 33−38.
(45) Huang, X.; Christopher, B.; Chai, S.; Xie, X.; Luo, S.; Liang, S.; Pan, A. Cowpea-like N-Doped Silicon Oxycarbide/Carbon Nanofibers as Anodes for High-Performance Lithium-Ion Batteries. *ACS Appl. Energy Mater.* **2021**, *4*, 1677−1686.
(46) Yue, Y.; Liang, H. 3D Current Collectors for Lithium-Ion Batteries: A Topical Review. *Small Methods* **2018**, *2*, 1800056.
(47) Zhu, P.; Gastol, D.; Marshall, J.; Sommerville, R.; Goodship, V.; Kendrick, E. A Review of Current Collectors for Lithium-Ion Batteries. *J. Power Sources* **2021**, *485*, No. 229321.
(48) Nyamaa, O.; Bae, J.-H.; Seo, D.; Jeong, H.-M.; Huh, S.-C.; Yang, J.-H.; Dolgor, E.; Noh, J.-P. Electrochemical Performance of Si Thin-Film with Buckypaper for Flexible Lithium-Ion Batteries. *Diamond Relat. Mater.* **2021**, *115*, No. 108351.
(49) Nyamaa, O.; Seo, D.-H.; Lee, J.-S.; Jeong, H.-M.; Huh, S.-C.; Yang, J.-H.; Dolgor, E.; Noh, J.-P. High Electrochemical Performance Silicon Thin-Film Free-Standing Electrodes Based on Buckypaper for Flexible Lithium-Ion Batteries. *Materials* **2021**, *14*, 2053.
(50) Chiluwal, S.; Sapkota, N.; Rao, A. M.; Podila, R. Three-Dimensional Si Anodes with Fast Diffusion, High Capacity, High Rate Capability, and Long Cycle Life. *ACS Appl. Mater. Interfaces* **2020**, *12*, 34763−34770.
(51) Gangadhar, J.; Maheshwari, A.; Bordia, R. K.; Shyam Kumar, C. N.; Kubel, C.; Sujith, R. Role of Carbon on the Thermal and Electrical Properties of Graphene- Enriched Silicon Oxycarbides. *Ceram. Int.* **2020**, *46*, 28156−28164.
(52) Chauhan, P. K.; Sujith, R.; Parameshwaran, R.; Prasad, A. V. S. S. Role of Polysiloxanes in the Synthesis of Aligned Porous Silicon Oxycarbide Ceramics. *Ceram. Int.* **2019**, *45*, 8150−8156.
(53) Ahn, D.; Raj, R. Cyclic Stability and C-Rate Performance of Amorphous Silicon and Carbon Based Anodes for Electrochemical Storage of Lithium. *J. Power Sources* **2011**, *196*, 2179−2186.
(54) Bahloul-Hourlier, D.; Latournerie, J.; Dempsey, P. Reaction Pathways during the Thermal Conversion of Polysiloxane Precursors into Oxycarbide Ceramics. *J. Eur. Ceram. Soc.* **2005**, *25*, 979−985.
(55) Wilamowska, M.; Pradeep, V. S.; Graczyk-Zajac, M.; Riedel, R.; Sorarù, G. D. Tailoring of SiOC Composition as a Way to Better Performing Anodes for Li-Ion Batteries. *Solid State Ionics* **2014**, *260*, 94−100.
(56) Brequel, H.; Parmentier, J.; Walter, S.; Badheka, R.; Trimmel, G.; Masse, S.; Latournerie, J.; Dempsey, P.; Turquat, C.; Desmartin-Chomel, A.; Neindre-Prum, L.; Jayasooriya, U. A.; Hourlier, D.; Kleebe, H.-J.; Soraru, G. D.; Enzo, S.; Babonneau, F. Systematic Structural Characterization of the High Temperature Behaviour of Nearly Stoichiometric Silicon Oxycarbide Glasses. *Chem. Mater.* **2004**, *16*, 2585−2598.
(57) Stabler, C.; Reitz, A.; Stein, P.; Albert, B.; Riedel, R.; Ionescu, E. Thermal Properties of SiOC Glasses and Glass Ceramics at Eevated Temperatures. *Materials* **2018**, *11*, 279.
(58) Mera, G.; Riedel, R.; Poli, F.; Müller, K. Carbon-Rich SiCN Ceramics Derived from Phenyl-Containing Poly(Silylcarbodiimides). *J. Eur. Ceram. Soc.* **2009**, *29*, 2873−2883.
(59) Sujith, R.; Chauhan, P. K.; Gangadhar, J.; Maheshwari, A. Graphene Nanoplatelets as Nanofillers in Mesoporous Silicon Oxycarbide Polymer Derived Ceramics. *Sci. Rep.* **2018**, *8*, 17633.
(60) Cançado, L. G.; Jorio, A.; Ferreira, E. H. M.; Stavale, F.; Achete, C. A.; Capaz, R. B.; Moutinho, M. V. O.; Lombardo, A.; Kulmala, T. S.; Ferrari, A. C. Quantifying Defects in Graphene via Raman Spectroscopy at Different Excitation Energies. *Nano Lett.* **2011**, *11*, 3190−3196.

https://doi.org/10.1021/acsami.3c00571
ACS Appl. Mater. Interfaces 2023, 15, 30039−30051

(61) Cançado, L. G.; Takai, K.; Enoki, T.; Endo, M.; Kim, Y. A.; Mizusaki, H.; Jorio, A.; Coelho, L. N.; Magalhães-Paniago, R.; Pimenta, M. A. General Equation for the Determination of the Crystallite Size La of Nanographite by Raman Spectroscopy. *Appl. Phys. Lett.* **2006**, *88*, 163106.
(62) Stabler, C.; Reitz, A.; Stein, P.; Albert, B.; Riedel, R.; Ionescu, E. Thermal Properties of SiOC Glasses and Glass Ceramics at Elevated Temperatures. *Materials* **2018**, *11*, 279.
(63) Shi, H.; Xie, Z.; Zhang, Y.; Yuan, A.; Xu, J. A SiOC Anode Material Derived from PVA-Modified Polysiloxane with Improved Li-Storage Cycling Stability. *Ionics* **2019**, *25*, 3051−3058.
(64) Xia, Y.; Cai, S.; Lu, C.; Huang, H.; Gan, Y.; Zhang, J.; Liang, C.; Xiao, Z.; Zhang, W. Rose Pollens as Sustainable Biotemplates for Porous SiOC Microellipsoids with Enhanced Lithium Storage Performance. *J. Alloys Compd.* **2020**, *816*, No. 152595.
(65) Xia, K.; Liu, X.; Liu, H.; Lu, Y.; Liu, Z.; Li, Y.; Duan, L.; Hou, Z.; Li, R.; Wang, D. Carbon-Enriched SiOC Ceramics with Hierarchical Porous Structure as Anodes for Lithium Storage. *Electrochim. Acta* **2021**, *372*, No. 137899.
(66) Mujib, S. B.; Ribot, F.; Gervais, C.; Singh, G. Self-Supporting Carbon-Rich SiOC Ceramic Electrodes for Lithium-Ion Batteries and Aqueous Supercapacitors. *RSC Adv.* **2021**, *11*, 35440−35454.
(67) Widgeon, S. J.; Sen, S.; Mera, G.; Ionescu, E.; Riedel, R.; Navrotsky, A. 29Si and 13C Solid-State NMR Spectroscopic Study of Nanometer-Scale Structure and Mass Fractal Characteristics of Amorphous Polymer Derived Silicon Oxycarbide Ceramics. *Chem. Mater.* **2010**, *22*, 6221−6228.
(68) Kleebe, H.-J.; Gregori, G.; Babonneau, F.; Blum, Y. D.; MacQueen, D. B.; Masse, S. Evolution of C-rich SiOC ceramics: Part I. Characterization by integral spectroscopic techniques: Solid-state NMR and Raman spectroscopy. *Int. J. Mater. Res.* **2006**, *97*, 699−709.
(69) Joy, R.; Balakrishnan, N. T. M.; Das, A.; Shafeek, S.; Thakur, V. K.; Zaghib, K.; Jaffarali, J. F. M.; Reddy, M. V. V.; Raghavan, P. Graphene: Chemistry and Applications for Lithium-Ion Batteries. *Electrochemistry* **2022**, *3*, 143−183.
(70) Maheshwari, A.; Gopikrishnan, E. P.; Gangadhar, J.; Sujith, R. Highly Conducting Graphene Dispersed Silicon Oxycarbide Glasses. *Mater. Chem. Phys.* **2020**, *239*, No. 121963.
(71) Weinberger, M.; Pfeifer, C.; Schindler, S.; Diemant, T.; Behm, R. J.; Wohlfahrt-Mehrens, M. Submicron-Sized Silicon Oxycarbide Spheres as Anodes for Alkali Ion Batteries. *J. Mater. Chem. A* **2015**, *3*, 23707−23715.
(72) Li, L.; Yang, H.; Zhou, D.; Zhou, Y. Progress in Application of CNTs in Lithium-Ion Batteries. *J. Nanomater.* **2014**, *2014*, No. 187891.
(73) Dong, B.; Han, Y.; Wang, T.; Lei, Z.; Chen, Y.; Wang, F.; Abadikhah, H.; Khan, S. A.; Hao, L.; Xu, X.; Cao, R.; Yin, L.; Agathopoulos, S. Hard SiOC Microbeads as a High-Performance Lithium-Ion Battery Anode. *ACS Appl. Energy Mater.* **2020**, *3*, 10183−10191.

https://doi.org/10.1021/acsami.3c00571
ACS Appl. Mater. Interfaces 2023, 15, 30039−30051